



Research Paper

The effects of TiN nanoparticle incorporation on the microstructure and wear resistance of additively manufactured CoCrMoW alloys

Canjuan Xiao^a, Wenting Jiang^{a,b}, Yi Huang^{c,d} , Song Ni^{a,*}

^a State Key Laboratory of Powder Metallurgy, Central South University, Changsha, 410083, China

^b College of Materials and Advanced Manufacturing, Hunan University of Technology, Zhuzhou, 412007, China

^c Department of Design and Engineering, Faculty of Science and Technology, Bournemouth University, Dorset, Poole, BH12 5BB, UK

^d Materials Research Group, Department of Mechanical Engineering, University of Southampton, Southampton, SO17 1BJ, UK



ARTICLE INFO

Keywords:

CoCrMoW alloy
Laser powder bed fusion
TiN nanoparticles
Wear resistance

ABSTRACT

To enhance the wear resistance of CoCrMoW alloys, this study used laser powder bed fusion (LPBF) to fabricate TiN nanoparticle-incorporated composites. By conducting microstructure characterization and wear resistance testing, the intricate relationship between microstructure and wear behavior was elucidated. The LPBF-fabricated samples presented dual-phase structures comprising face-centered cubic and hexagonal close-packed phases along with numerous stacking faults. The TiN particles were uniformly distributed in the sample with a 1 wt% addition. However, as the additive content increased, the TiN particles grew, and the interparticle spacing correspondingly decreased. Notably, robust interfacial bonding existed between the TiN nanoparticles and the matrix material. The interface between the TiN particles and the matrix displayed a semicoherent nature characterized by a specific orientation relationship: $[001]_{\text{TiN}} // [011]_{\gamma}$ and $(020)_{\text{TiN}} // (111)_{\gamma}$. Compared to the nonincorporated sample, the incorporated samples demonstrated reduced friction coefficients and wear rates. A comparative analysis of the nonincorporated and incorporated samples' wear behaviors revealed that oxidation wear predominantly characterized the nonincorporated sample, which displayed significant plastic deformation along with fragmented debris and loose oxides. In contrast, the incorporated samples presented relatively smooth wear surfaces where abrasive wear emerged as the primary mechanism. These findings underscore enhancements in tribological properties due to TiN incorporation and offer valuable insights into its fundamental behavior during wear.

1. Introduction

Cobalt-chromium-molybdenum (CCM) alloys are extensively utilized in biomedical orthopedic implants due to their high strength, exceptional corrosion resistance, and biocompatibility [1,2]. CCM alloys typically exhibit a dual-phase structure consisting of a hexagonal close-packed phase (ϵ -HCP phase), which is a hard, brittle martensitic transformation product, and a face-centered cubic phase (γ -FCC phase) that serves as the soft matrix [3,4]. These alloys are generally produced via casting, which is a process that often results in multiscale defects, such as coarse dendritic microstructures and carbide precipitation. These defects negatively impact the overall performance of CCM alloys, particularly in terms of strength and ductility [5–7].

Laser powder bed fusion (LPBF), an advanced additive

manufacturing (AM) technique, is widely used to produce materials with exceptional properties and intricate geometries [8,9]. This process employs a high-energy laser beam to melt metal powders and enable layer-by-layer fabrication of dense metal components. LPBF offers significant advantages including its ability to customize components for personalized biomedical devices [10,11].

Advancements in AM technology have enabled CCM alloys produced via the LPBF process to achieve superior strength, which is attributed to the high-energy input and rapid cooling rates inherent in this method [12–14]. Thus, LPBF technology has gained widespread application in the fabrication of biological implants [15]. However, orthopedic implants inevitably generate friction with surrounding bone tissue, which can lead to sterile loosening of an implant and reduced lifespan [16,17]. Consequently, enhancing the wear properties of CCM alloys is critically

Peer review under the responsibility of Editorial Board of Smart Materials in Manufacturing

* Corresponding author.

E-mail address: song.ni@csu.edu.cn (S. Ni).

<https://doi.org/10.1016/j.smmf.2025.100078>

Received 15 November 2024; Received in revised form 10 March 2025; Accepted 11 March 2025

Available online 22 March 2025

2772-8102/© 2025 The Authors. Publishing services by Elsevier B.V. on behalf of KeAi Communications Co. Ltd. This is an open access article under the CC BY-NC-ND license (<http://creativecommons.org/licenses/by-nc-nd/4.0/>).

important.

Hard ceramic particles, such as TiC, TiN, B₄C, and SiC, are frequently employed as reinforcement materials [18–21]. This is because of their high hardness and excellent wear resistance, which significantly influence composites' mechanical and physical characteristics [22,23]. A considerable number of studies have demonstrated that the incorporation of ceramic particles can influence the physical properties, mechanical properties, and microstructure of composites. For instance, Song et al. [24] investigated the AM behavior of SiC/Fe bulk nanocomposites and disclosed that adding SiC to the Fe matrix significantly enhanced viscosity and local melt instability. The fabricated Fe/SiC nanocomposite samples exhibited much higher strength and improved tensile properties compared to the pure iron samples.

Li et al. [25] studied TiN/IN718 composites fabricated using LPBF. They discovered that the addition of TiN could refine the grains, enhance the texture strength, reduce the detrimental precipitation of the Laves phase, and considerably improve the favorable combination of strength and plasticity of the composite. Additionally, the added second-phase particles might decompose or precipitate in situ during the AM process. For example, Thapliyal et al. [26] examined B₄C-reinforced Fe-Mn-Co-Cr-Si high-entropy alloys produced by LPBF. B₄C decomposes during the LPBF process and leads to the segregation of the B element at the grain boundary. Zhai et al. [27] reinforced 316L stainless steel with micron-sized TiC particles using LPBF. Despite the addition of micron-sized TiC particles, in-situ precipitated nanoscale TiC particles were dispersed throughout the matrix, indicating partial melting or decomposition of TiC during the LPBF process. Pan et al. [28] prepared a TiC-strengthened CoCrNi medium entropy alloy. They found that TiC broke down during LPBF, forming a Cr₂₃C₆ phase at the cell substructure boundary. Moreover, TiO₂/TiC nanoprecipitates with TiO₂ as the core were also identified, which were considered to be caused by the partial oxidation of TiC during in-situ formation. In summary, the addition of ceramic particles to different alloys produces a variety of reactions and affects both microstructures and properties.

The incorporation of ceramic particles has been recognized as an effective strategy for enhancing materials' frictional properties. For example, Gu et al. [20] synthesized high-entropy alloys with varying levels of SiC incorporation. Among these, samples containing 1 vol% SiC exhibited the lowest average friction coefficient and wear rate, primarily undergoing abrasive wear. Compared to nonincorporated samples, these alloys showed significant improvements in tribological performance. Similarly, Cao et al. [16] produced Al₂O₃-doped CCM alloys via LPBF processing and assessed their tribological properties. At an incorporation level of 1 wt%, the alloy demonstrated the smallest wear track width and stable friction coefficients. Li et al. [25] investigated the tribological properties of TiN/IN718 composites fabricated with LPBF. They found that composites with a 3 wt% TiN content exhibited excellent tribological performance, with a friction coefficient of 0.531 and wear mass reduced to half that of IN718. These results highlight TiN's notable abrasion and wear resistance within composites.

Currently, research on CCM alloys is mainly concentrated on enhancing their mechanical properties [17,29,30]. Although several studies have demonstrated that adding ceramic particles can somewhat improve the tribological properties of CCM alloys [16,31–33], a comprehensive understanding of particle effects and the relationship between a microstructure and its wear behavior remains insufficiently explored. A key issue is determining which kind of ceramic material should be selected as the reinforcement. In numerous studies, nitrogen (N) incorporation (achieved by the addition of Cr₂N powders or melting/gas atomization in a nitrogen atmosphere) has been widely employed to strengthen CCM alloys, yielding significant advancements [29,34,35]. Due to its excellent biocompatibility, high hardness, and wear resistance, TiN has been regarded as an ideal choice for antiwear protection of load-bearing biomaterials and has been extensively applied in cardiovascular and orthopedic implants [36–40].

In this current study, TiN-incorporated CoCrMoW alloys were

fabricated using the LPBF method, taking advantage of the excellent biocompatibility of both Ti and N. Microstructural characteristics were analyzed and dry sliding wear tests were conducted to assess the influence of TiN particle incorporation on wear behavior.

2. Experimental procedure

In this experiment, gas-atomized CoCrMoW powder (Chengdu Kewan Intelligent Technology Co., Ltd., China), with a particle size of 20–60 μm, was utilized (see Fig. 1a). The chemical composition measured by inductively coupled plasma was (in weight percent, wt.%): 27.53 % Cr, 5.19 % Mo, 5.35 % W, 0.55 % Si, 0.011 % Mn, and the balance Co. A scanning electron microscopy (SEM) energy dispersive spectrometry (EDS) analysis of a particle, shown in Fig. 1b, confirmed the uniform distribution of the principal elements.

Fig. 1c and d presents transmission electron microscopy (TEM) images of TiN powder alongside their corresponding Fast Fourier Transform (FFT) and Inverse Fast Fourier Transform (IFFT) spectra, revealing that TiN particles exhibit a spherical morphology. The TiN powder was blended with CoCrMoW powder using a solution-mixing method. Specifically, the TiN powder was first dispersed in alcohol via ultrasonic vibration followed by the addition of CoCrMoW powder. The mixture was subjected to electromagnetic stirring in a water bath until the alcohol completely evaporated. Finally, the mixed powder was dried in a vacuum-drying oven.

The SEM and EDS results of the mixed powders containing 1 wt% and 2 wt% TiN, shown in Fig. 1e and f, indicate that the TiN particles adhered uniformly to the surfaces of the CoCrMoW powder. The nanoscale TiN particles tended to adhere to the surfaces of the micronscale CoCrMoW particles during the solution mixing and drying process, driven by electrostatic adsorption. For simplicity, the pure CoCrMoW alloy and the TiN/CoCrMoW composites that contain 1 wt% and 2 wt% TiN are henceforth referred to as CCM-0, CCM-1, and CCM-2, respectively.

The LPBF process was conducted using a DiMetal-150 L machine (Laseradd, China) under argon gas protection, ensuring an oxygen content below 500 ppm. Process parameters were optimized via a series of orthogonal experiments, varying laser power, hatch spacing, and scanning speed, and were subsequently finalized as follows based on assessments of relative density and mechanical properties: 220 W of laser power, 0.07 mm of hatch spacing, a 950 mm/s scanning speed, and a 0.03 mm layer thickness. The scanning direction alternated by 67° between consecutive layers, achieving a total height of approximately 2 mm.

The microstructures of all specimens were characterized by optical microscopy (OM), SEM (Model Quanta 250 FEG), and TEM (Titan G2 FEI). OM and SEM specimens were prepared by sandpaper grinding, polished using W2.5, W1.5, and W0.5 diamond polishing paste, and finally polished with 0.02 μm silica polishing solution. TEM samples were electropolished using a twin-jet method in a mixed solution of 5 % perchloric acid and 95 % alcohol, with an applied voltage of 30 V and a temperature of –25 °C. Phase constitutions were identified via X-ray diffraction (XRD) using Cu Kα radiation with a D8 ADVANCE apparatus.

Wear tests were conducted using a ball-on-disk device (UMT-3) under dry sliding conditions. 60 N was applied during the tests on a 10 mm liner line with a reciprocating frequency of 300 times per minute for a duration of 30 min. A 9.5 mm Si₃N₄ ball served as the abrasive tip. Wear tracks and local macroscopic three-dimensional (3D) topography were analyzed using SEM and a laser spectroscopy confocal microscope (KC-X1000, China). Microhardness values were determined by averaging data from at least five locations using an HVS-1000M2 Vickers microhardness tester.

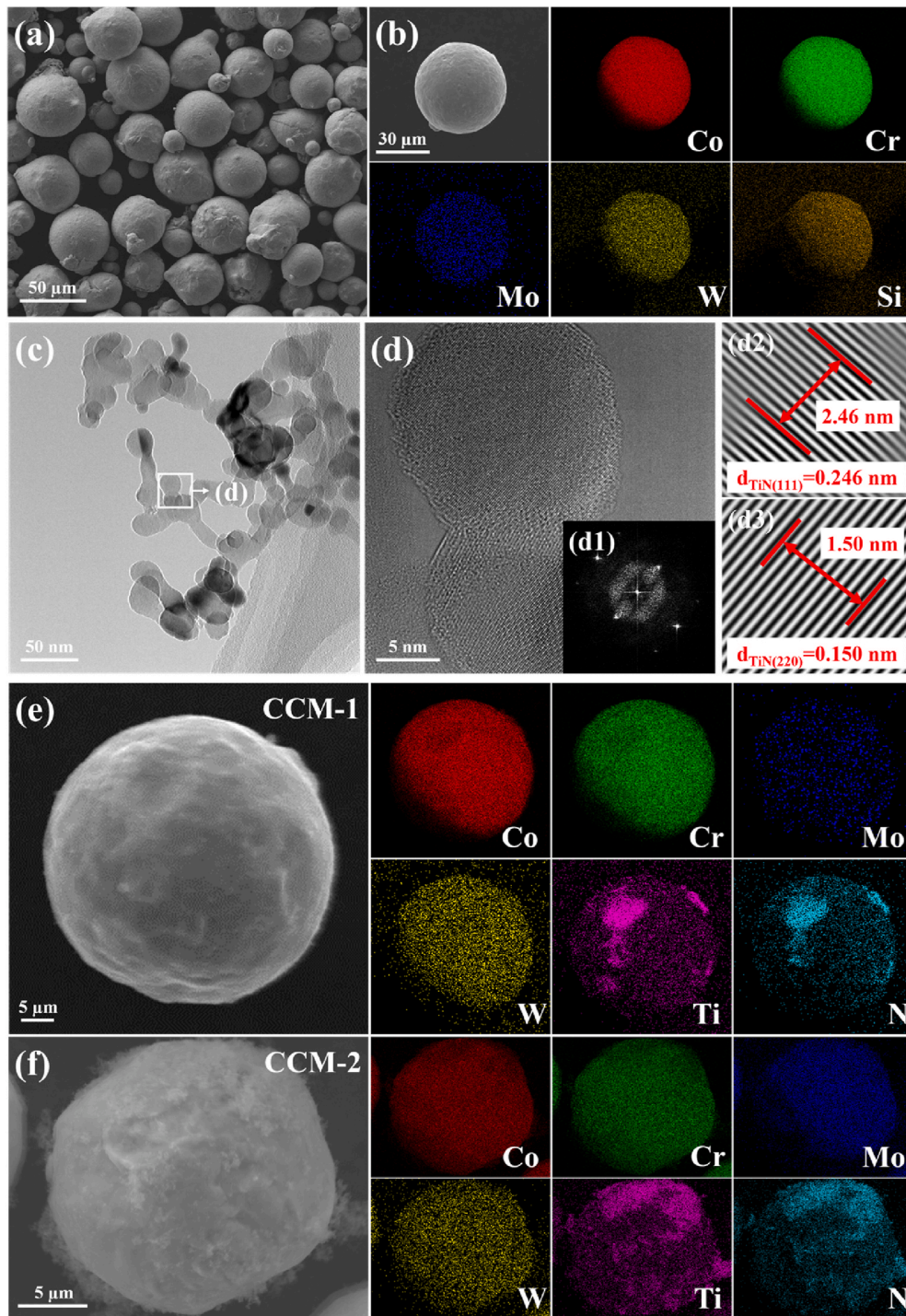


Fig. 1. (a) Morphology of the CoCrMoW powder; (b) SEM-EDS analysis of CoCrMoW particles; (c, d) TEM analysis of the TiN particles; (e, f) morphology and element distribution of the mixed powders.

3. Results

3.1. Microstructures of LPBF-ed alloys

Fig. 2 presents OM images of the nonincorporated and incorporated samples. The observation direction is parallel to the construction direction. It is evident that the molten pools, characterized by a flat slat configuration, are approximately 70 μm apart, aligning with the specified parameters. The bond between adjacent pools is exceptionally tight, resulting in well-formed samples under these LPBF process conditions.

The relative densities of the three samples were 99.24 % for CCM-0, 99.20 % for CCM-1, and 99.35 % for CCM-2.

Fig. 3(a–c) shows the electron backscattered diffraction (EBSD) inverse pole figures and XRD patterns of the three samples. According to EBSD grain size statistics, the average grain sizes of CCM-0, CCM-1, and CCM-2 are 32.27 μm , 34.98 μm , and 30.33 μm , respectively, which shows no obvious change in grain size. The XRD patterns reveal the presence of both the FCC and HCP phases in all three samples. The ratio of the integrated intensities of the $(200)_{\text{fcc}}$ and $(10\bar{1}1)_{\text{hcp}}$ diffraction peaks, which serve as an indicator of the relative phase content [41],

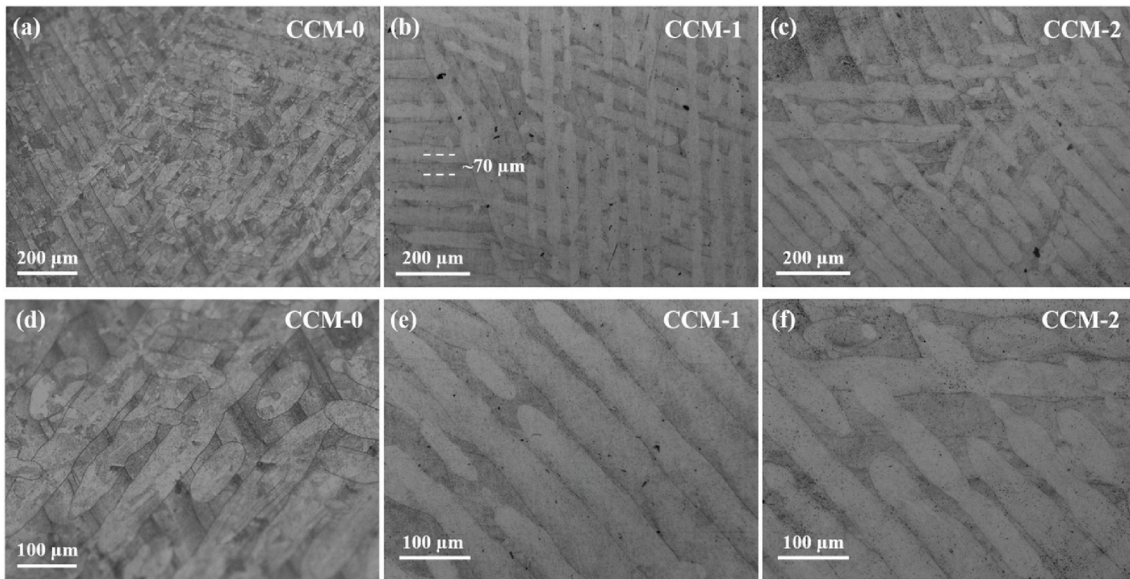


Fig. 2. OM images of the samples: (a, d) CCM-0, (b, e) CCM-1, and (c, f) CCM-2.

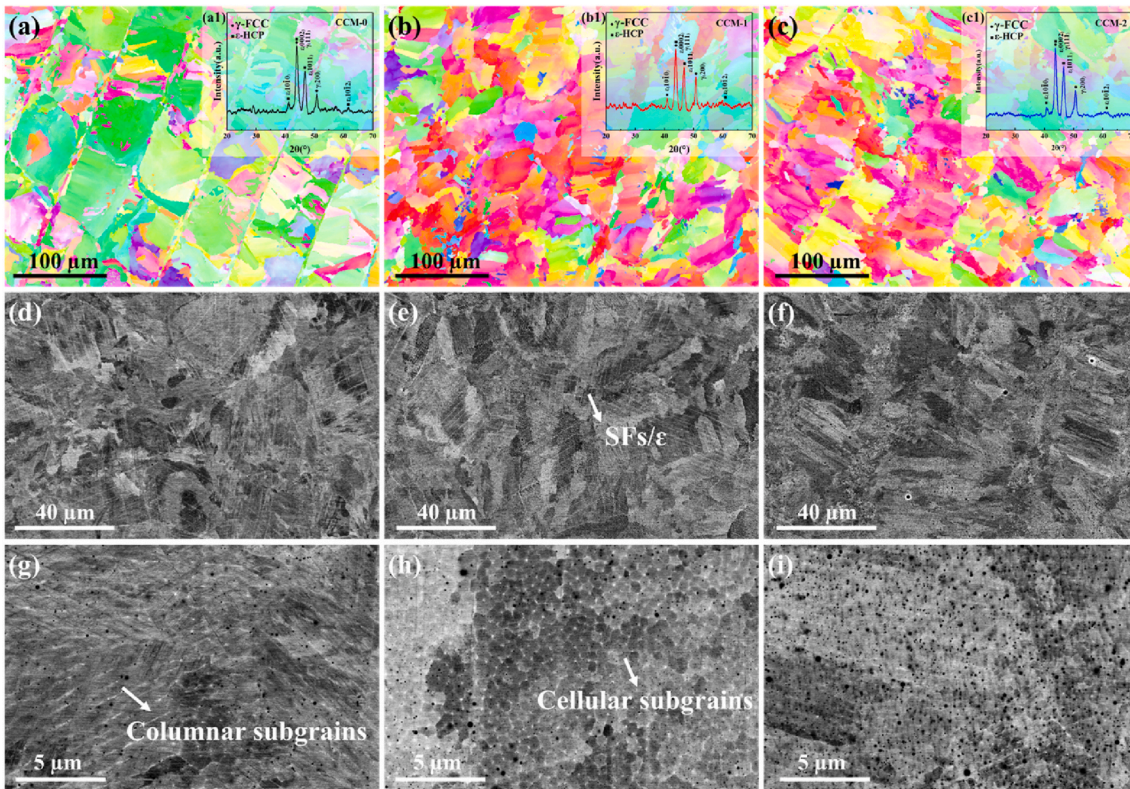


Fig. 3. EBSD, XRD, and ECC images of the samples: (a, d, g) CCM-0, (b, e, h) CCM-1, and (c, f, i) CCM-2.

shows a gentle increase with the addition of TiN. This suggests that the addition of TiN moderately suppressed the γ -to- ϵ transformation, but the effect was not pronounced.

As illustrated in Fig. 3d–f, a significant number of stacking faults (SFs) and thin ϵ -HCP lamellae are present in the as-built samples alongside cellular and columnar subcrystals formed under rapid cooling conditions during the LPBF process [42]. Constitutional supercooling, represented by the G/R ratio (G: temperature gradient and R: solidification rate), influences the formation of cellular and columnar subgrains. During the LPBF process, the columnar subgrains epitaxially

grow perpendicular to the melt pool boundary due to the orientation of the temperature gradient. As solidification advances, the liquid–solid interface transitions from the bottom to the top of the melt pool, leading to a decrease in the G/R ratio at the top, where cellular subgrains are formed [43–45].

Furthermore, as shown in Fig. 3g–i, increasing the incorporation concentration leads to noticeable changes in the size and distribution of second-phase particles. In the CCM-0 sample, a small number of oxide particles are dispersed within the matrix. In contrast, the CCM-1 sample exhibits finely dispersed TiN particles that are uniformly distributed

throughout the cell structure and along grain boundaries. This phenomenon can be attributed to surface tension gradients induced by local temperature variations and chemical concentration gradients within a liquid molten pool during LPBF processing, which facilitate Marangoni flow within that environment. Such convection enhances particle movement and rearrangement [46,47]. In the sample, when the incorporation level reaches 2 wt%, a noticeable increase in both the size and nonuniformity of second-phase particles is observed.

Fig. 4 presents bright-field TEM and high-resolution TEM images of the CCM-0 sample, revealing dual-phase structures comprising γ -FCC and ϵ -HCP along with numerous SFs. The FFT image depicted in Fig. 4a1 illustrates the orientation relationships between thin ϵ laths and γ matrix that conforms to the Schmid-Nabarro rules: $\{111\}_{\gamma}/\{0001\}_{\epsilon}$ and $\langle 110 \rangle_{\gamma}/\langle 11,20 \rangle_{\epsilon}$ [48]. It can be seen that a large number of SFs or thin ϵ laths intersect, forming a complex network. The high-resolution TEM image in Fig. 4b shows the different lattice structures of the γ and ϵ phases. Furthermore, Fig. 4c and d illustrate the cellular and columnar subgrain structures, respectively, which represent the distinctive microstructure characteristics of AM.

Fig. 5a illustrates a typical bright-field TEM image of the incorporated samples, showing a significant presence of SFs, thin ϵ -HCP phases, and secondary phase particles indicated by red arrows. Fig. 5a1 illustrates orientation relationships between thin ϵ laths and γ matrix that conforms to Schmid-Nabarro rules: $\{111\}_{\gamma}/\{0001\}_{\epsilon}$ and $\langle 110 \rangle_{\gamma}/\langle 11,20 \rangle_{\epsilon}$ [48]. Fig. 5b is a dark-field image of the region corresponding to Fig. 5a by selecting diffraction spots of ϵ -HCP matrix in Fig. 5a1 for imaging. The lamellas appearing bright are ϵ laths with a width of tens to hundreds of nanometers, as indicated by yellow arrows. Fig. 5c presents a HAADF-STEM image of the doped sample, revealing a significant presence of secondary phase particles, SFs/thin ϵ -HCP phases, and weak cellular substructures. The HAADF-STEM image presented in Fig. 5d, along with the corresponding EDS spectra, indicates that these particles are rich in Ti and N. Fig. 5e displays a high-resolution TEM image of a particle from Fig. 5d, while Fig. 5f provides an enlarged view of this particle.

Notably, it was observed that SFs within the matrix did not propagate through the particles. The identification of these particles as TiN was

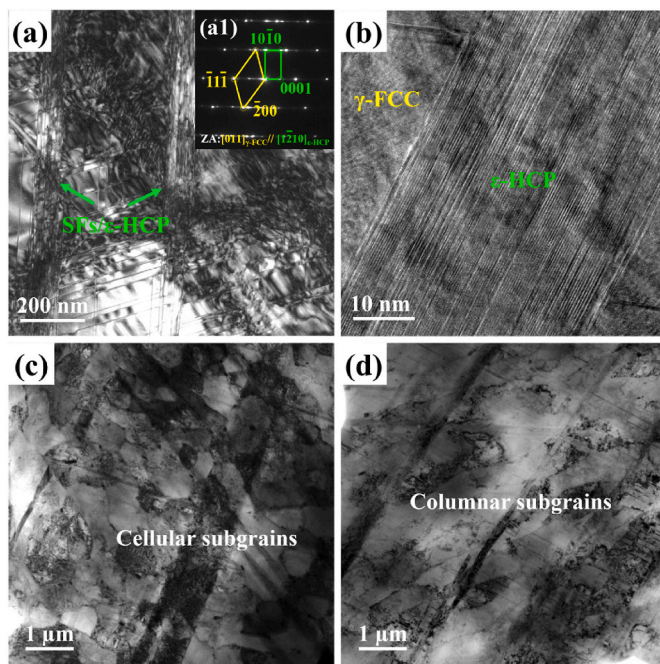


Fig. 4. (a, b) Bright-field and high-resolution TEM images showing the dual-phase structures comprising γ -FCC and ϵ -HCP phases; (c, d) bright-field TEM images showing the cellular and columnar subgrains of the CCM-0 sample.

confirmed via FFT processing and indexing. As shown in Fig. 5g, there exists a specific orientation relationship between TiN and the γ -FCC matrix: $[001]_{\text{TiN}}/[011]_{\gamma}$, $(0_{-20})_{\text{TiN}}/(11_1)_{\gamma}$. The interplanar distance between the (200) planes of the FCC matrix is measured to be ~ 0.175 nm, closely aligning with the theoretical value of 0.177 nm, as illustrated in Fig. 5g1. The interplanar spacing between the (200) planes of TiN is measured to be ~ 0.217 nm, close to its theoretical value of 0.212 nm.

3.2. Wear behaviors

Fig. 6 presents the friction coefficient (COF) values recorded during wear tests conducted on both nonincorporated and incorporated samples under a load of 60 N. The COF of the CCM-0 sample exhibited a gradual increase over time, indicating deteriorating wear conditions as friction progressed. Conversely, the incorporated samples displayed distinct behavior, where the COF values for CCM-1 and CCM-2 fluctuated slightly but tended toward stability over time. For the three samples, the average COF values were determined to be approximately 0.36, 0.30, and 0.29, respectively. Compared to the nonincorporated CCM-0 sample, the wear rates of the CCM-1 and CCM-2 samples decreased by 7.8 % and 15.5 %, respectively.

Al-Aloosi et al. [49] investigated the friction and wear performance of CCM alloys under various laser scanning speeds. Their results indicated that at a scanning speed of 700 mm/s, the lowest coefficient of friction (COF) value achieved was 0.36, which was significantly higher than the COF of 0.29 observed in this current study. These results suggest that incorporating TiN effectively reduces COF, thereby enhancing wear-resistance properties. Furthermore, the hardness of the nonincorporated sample increased from 455 HV to 542 HV in the CCM-1 sample, and when the incorporation concentration reached 2 wt%, the hardness further elevated to 567 HV.

Three-dimensional (3D) surface profiles alongside two-dimensional cross-sectional depth profiles for wear tracks are depicted in Fig. 7 (a–f). The averaged width and depth measurements for wear tracks across all three samples are approximately: 990 μm , 28 μm ; 972 μm , 26 μm ; 900 μm , 26 μm for CCM-0, CCM-1 and CCM-2 samples, respectively, which are summarized in Fig. 7g. The maximum width & depth were noted specifically within the CCM-0 sample. The average volume losses of the three specimens were calculated to be around $2.79 \times 10^{-2} \text{ mm}^3$, $2.56 \times 10^{-2} \text{ mm}^3$, and $2.36 \times 10^{-2} \text{ mm}^3$ respectively. As demonstrated in Fig. 7h, the corresponding average wear rates were about $2.58 \times 10^{-5} \text{ mm}^3/\text{N}\cdot\text{m}$, $2.38 \times 10^{-5} \text{ mm}^3/\text{N}\cdot\text{m}$, $2.18 \times 10^{-5} \text{ mm}^3/\text{N}\cdot\text{m}$. Compared to the nonincorporated CCM-0 sample, the wear rates of the CCM-1 and CCM-2 samples decreased by 7.8 % and 15.5 %, respectively. These volumetric loss results indicate that the incorporation of TiN substantially reduces wear and friction, contributing positively to improved performance characteristics.

3.3. Worn surfaces

Examining the morphology of worn surfaces provides valuable insights into wear mechanisms. Fig. 8 illustrates the morphology of the wear tracks. For all specimens, the worn surfaces exhibited plastic deformation characterized by delamination, with continuous dark tribofilms present at the centers of the wear tracks, indicating direct contact between the worn surface and Si_3N_4 . Additionally, as depicted in Fig. 8a, the surface of the CCM-0 sample displays significant plastic deformation along with deep wear grooves and large debris particles. Further analysis using EDS elemental mapping confirmed that this debris consists primarily of oxides—typical characteristics associated with oxide wear. The oxide on the worn surface forms as a result of a chemical reaction between the metal surface and oxygen in the air during the wear test. The oxides generated during wear tended to adhere poorly to substrates, leading to their degradation and transformation into new friction particles, which exacerbated surface wear on the

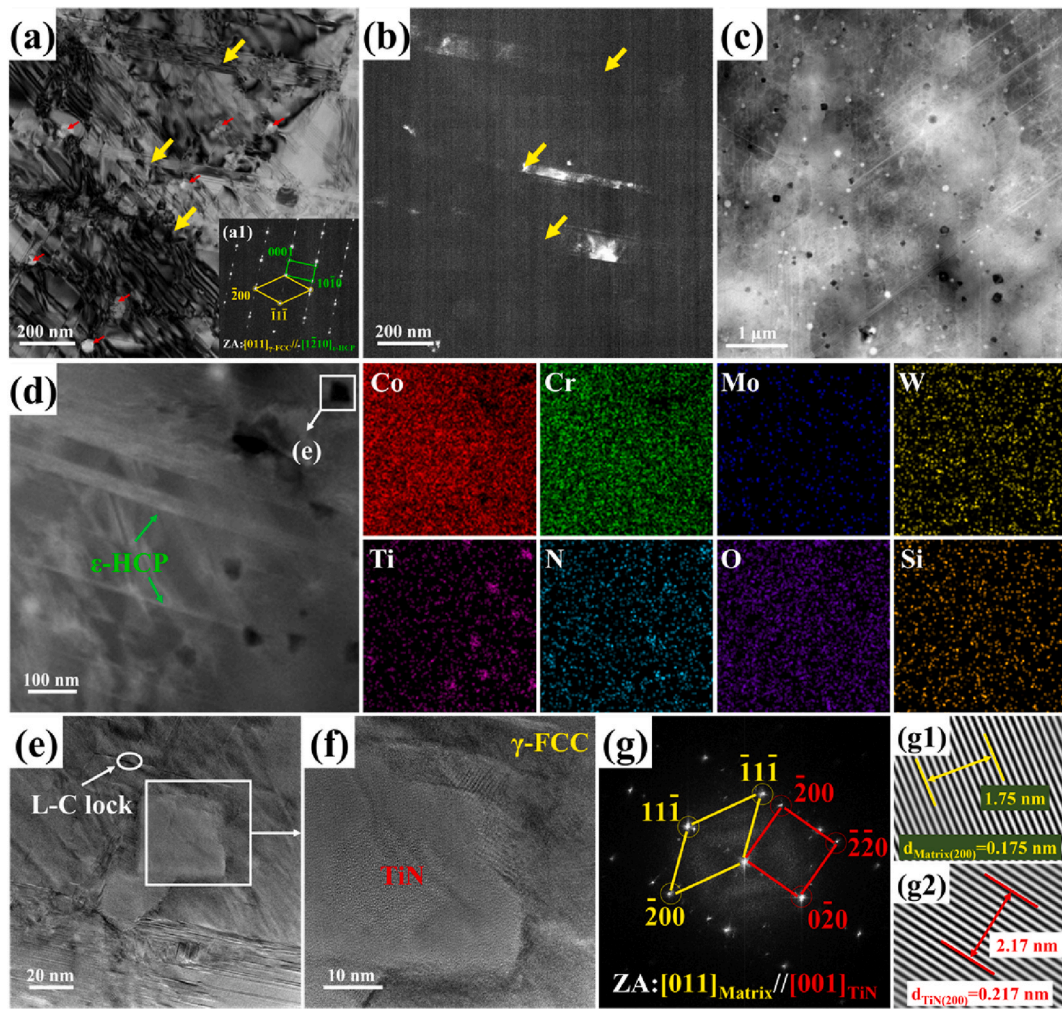


Fig. 5. (a) A bright-field TEM image of the incorporated samples; (b) a dark-field TEM image of the incorporated samples; (c) an HADDF-STEM image of the incorporated samples; (d) an HADDF-STEM image and its corresponding EDS mappings; (e, f) high-resolution HAADF images of a particle; (g) FFT and IFFT patterns of (f).

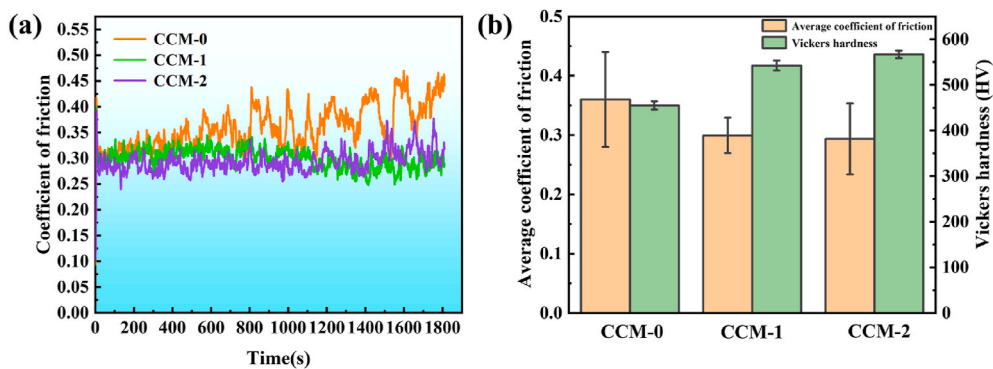


Fig. 6. (a) COF versus time (s) for CCM-0, CCM-1, and CCM-2 samples with loads of 60 N; (b) histogram of averaged COF summarized from (a) and Vickers hardness values.

samples [50].

As shown in Fig. 8(b and c), the wear tracks for CCM-1 and CCM-2 exhibit extensive continuous friction films accompanied by significantly reduced groove depths and limited surface damage areas. This behavior contributes to maintaining a stable COF. It can be concluded that abrasive wear is the predominant mechanism affecting the incorporated samples. The corresponding EDS analyses revealed a notable

reduction in oxide content alongside a more uniform distribution across these samples. Furthermore, the accumulation of Ti and N elements was observed on both the CCM-1 and CCM-2 surfaces, likely originating from TiN particles. The Ti enrichment of CCM-1 is very weak, which may be attributed to the smaller particle size observed in CCM-1, as illustrated in Fig. 3. Both the CCM-1 and CCM-2 samples demonstrated high resistance to surface deformation when compared to their

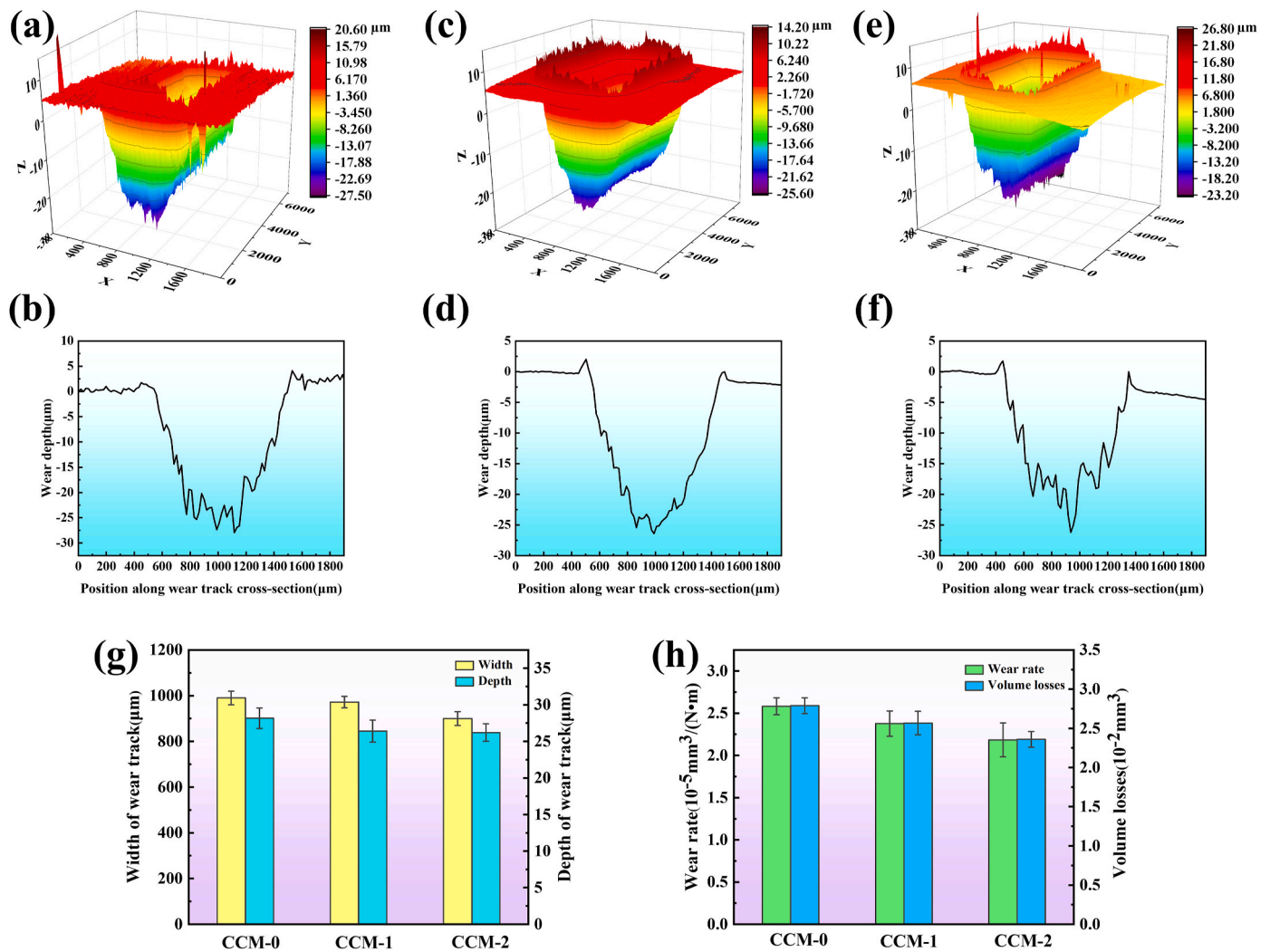


Fig. 7. (a–f) 3D surface profile and 2D cross-sectional depth profiles of the wear tracks of (a, b) CCM-0 (c, d) CCM-1; (e, f) CCM-2; (g) averaged width and depth of the wear tracks; (h) wear volume losses and wear rates of the three samples.

nonincorporated counterparts.

4. Discussion

The wear and tribological behavior of materials is governed by a complex interplay of factors, including a material's intrinsic physical properties and specific parameters employed during wear testing. Extensive research has been undertaken to enhance wear resistance via various surface treatments, such as nitriding, boriding, and aluminum plating [51–54]. These methods aim to introduce a durable second phase and modify the microstructure of a material, thereby improving its frictional performance [55–57].

In this current study, incorporating TiN resulted in an increase in hardness from approximately 455 HV in sample CCM-0 to about 542 HV in sample CCM-1 and around 567 HV in sample CCM-2. By comparing the morphology of TiN particles and their orientation relationships with the matrix alloy before and after the LPBF process, it can be inferred that TiN underwent a process of melting and reprecipitation during the printing process. The initial TiN particles had a spherical morphology. Under laser irradiation, the initially spherical TiN particles underwent melting and reprecipitation, transforming into square-shaped particles in the LPBF-processed sample and exhibiting a specific orientation relationship with the matrix.

TiN, as a ceramic reinforcement phase, is inherently very hard.

Additionally, its strong bonding with the CoCrMoW alloys matrix makes it difficult to detach from the matrix, resulting in high hardness. Notably, a positive correlation exists between wear properties and hardness [58]. This tough second phase enhances material hardness and leverages TiN's inherent wear resistance capabilities, significantly augmenting overall wear performance. Furthermore, the specific orientation relationship between TiN particles and the FCC matrix, as well as the semi-coherent interface between them, reduces the likelihood of TiN particles detaching from the matrix during wear experiments. This characteristic significantly enhances wear resistance. As TiN content increases, particle spacing decreases and reduces the frontal contact area between the matrix and the friction pair. During frictional interactions, TiN particles bear loads, which leads to a transition in wear mechanisms from abrasive and oxidative processes to predominantly abrasive wear.

In the nonincorporated CCM-0 sample, the primary wear characteristics include severe plastic deformation accompanied by loose spalling oxides. In contrast, the incorporated CoCrMoW alloys exhibited relatively smooth worn surfaces. This difference arose because in the CCM-0 sample, the matrix surface lacked the protection of a reinforcing TiN phase, resulting in lower hardness. Consequently, the wear debris acted as abrasive particles, embedding them into the matrix and accelerating surface damage. The incorporation of TiN played a crucial role in enhancing wear resistance as the particles absorbed the primary load and resisted abrasive forces, which is consistent with the observed

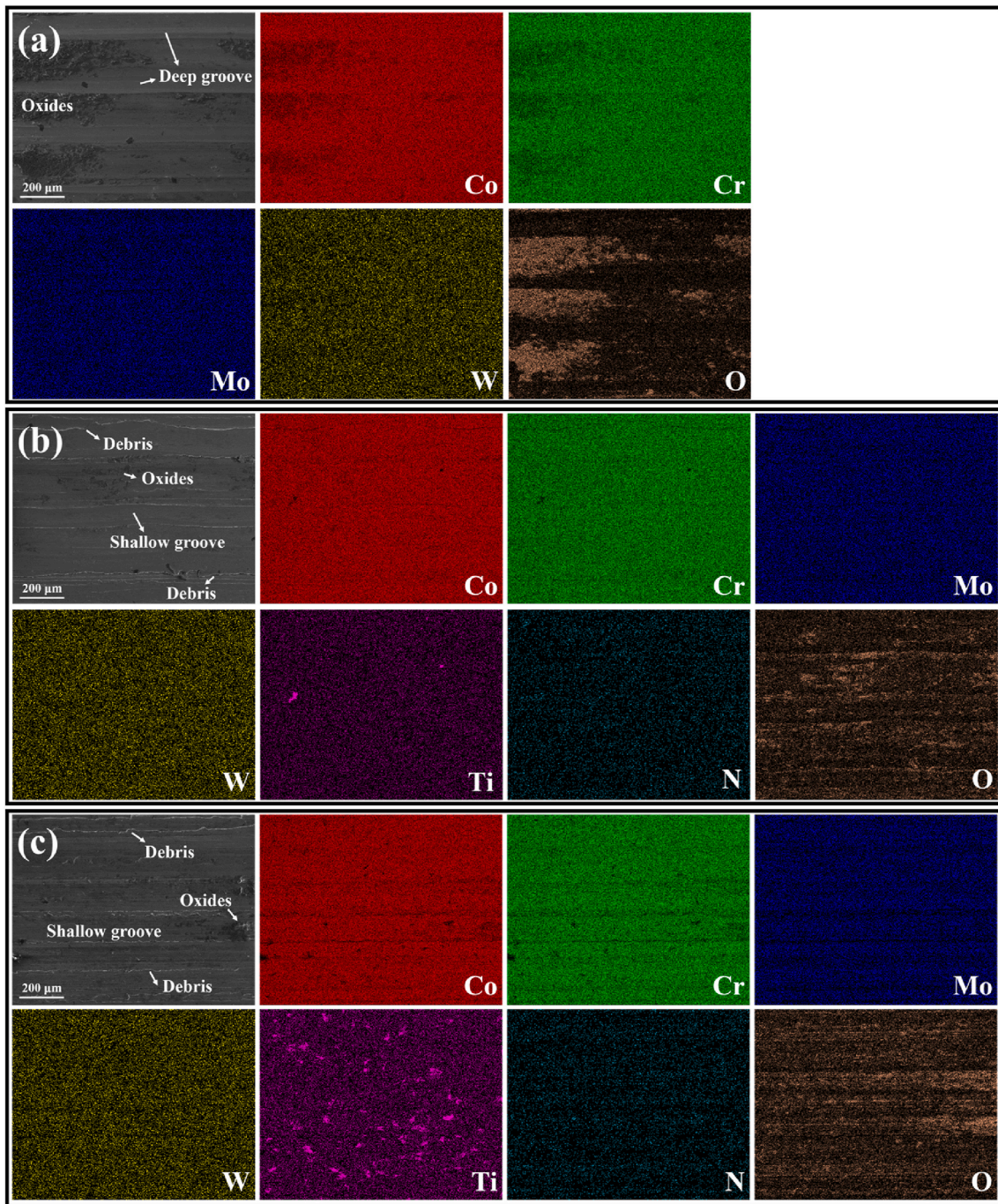


Fig. 8. Surface morphology and composition of the three samples after dry sliding against Si₃N₄ under 60 N; (a) CCM-0 sample; (b) CCM-1 sample; (c) CCM-2 sample.

macroscopic morphology. Notably, the wear resistance of the CCM-2 sample was further improved compared to CCM-1, as the higher TiN content allowed more particles to absorb the load and resist deformation and wear.

5. Conclusion

In this study, TiN-incorporated CoCrMoW composites were successfully prepared using the solution-mixing method and the LPBF process. Microstructures were thoroughly characterized, and wear resistance and wear behavior were studied in detail. The key findings are summarized as follows.

- (1) The LPBF-ed samples presented a dual-phase structure comprising γ -FCC and ϵ -HCP along with numerous SFs. The TiN particles in the CCM-1 sample exhibited a finely dispersed distribution. As the TiN content rose to 2 wt% (CCM-2 sample), the particle size increased while the interparticle spacing decreased. The interface between the TiN particles and the matrix displayed a semicoherent nature with a specific orientation relationship: $[001]_{\text{TiN}}//[011]_{\gamma}$ and $(020)_{\text{TiN}}//(\bar{1}11)_{\gamma}$.
- (2) A significant enhancement in wear resistance was observed. Specifically, the COF and wear rates of the CCM-2 samples decreased by 19.4 % (from 0.36 to 0.29) and 15.5 % (from 2.58 mm³/N•m to 2.18 mm³/N•m), respectively, compared to the CCM-0 sample.

- (3) The wear mechanisms of the nonincorporated and incorporated samples differed notably. For the CCM-0 sample, oxidative wear was the dominant mechanism characterized by severe plastic deformation, the presence of wear debris, and the formation of loose oxides. Conversely, the incorporated samples exhibited abrasive wear as the primary mechanism, resulting in a relatively smooth wear surface.

This study demonstrates that the addition of TiN significantly enhances the wear resistance of CoCrMoW alloys, providing a promising approach to extending the service life of medical alloys.

CRedit authorship contribution statement

Canjuan Xiao: Writing – review & editing, Writing – original draft, Investigation, Formal analysis, Data curation. **Wenting Jiang:** Formal analysis, Data curation. **Yi Huang:** Writing – review & editing, Formal analysis. **Song Ni:** Writing – review & editing, Supervision, Project administration, Funding acquisition, Formal analysis, Conceptualization.

Declaration of competing interest

The author Song Ni is an Editorial Board Member for *Smart Materials in Manufacturing* and was not involved in the editorial review or the decision to publish this article.

Acknowledgments

The authors acknowledge financial support from the National Natural Science Foundation of China [grant number 52171130 (S. Ni)], the Huxiang Youth Talents Support Program [grant number 2021RC3002 (S. Ni)], and the Postgraduate Research Innovation Project of Center South University (2023ZZTS0769). Y. Huang is grateful for support from the Royal Society in the U.K. under Grant No. IES\R3\223190.

References

- Q. Chen, G.A. Thouas, Metallic implant biomaterials, *Mater. Sci. Eng. R Rep.* 87 (2015) 1–57.
- J.C. Wataha, Alloys for prosthodontic restorations, *J. Prosthet. Dent.* 87 (2002) 351–363.
- Z. He, N. Jia, H. Yan, Y. Shen, M. Zhu, X. Guan, X. Zhao, S. Jin, G. Sha, Y. Zhu, C. T. Liu, Multi-heterostructure and mechanical properties of N-doped FeMnCoCr high entropy alloy, *Int. J. Plast.* 139 (2021) 102965.
- C. Bonatti, D. Mohr, Large deformation response of additively-manufactured FCC metamaterials: from octet truss lattices towards continuous shell mesostructures, *Int. J. Plast.* 92 (2017) 122–147.
- A.J. Saldívar-García, H.F. López, Microstructural effects on the wear resistance of wrought and as-cast Co-Cr-Mo-C implant alloys, *J. Biomed. Mater. Res. Part. A.* 74 (2005) 269–274.
- K. Yamanaka, M. Mori, A. Chiba, Developing high strength and ductility in biomedical Co–Cr cast alloys by simultaneous doping with nitrogen and carbon, *Acta Biomater.* 31 (2016) 435–447.
- K. Yamanaka, M. Mori, A. Chiba, Influence of carbon addition on mechanical properties and microstructures of Ni-free Co–Cr–W alloys subjected to thermomechanical processing, *J. Mech. Behav. Biomed. Mater.* 37 (2014) 274–285.
- T. DebRoy, H.L. Wei, J.S. Zuback, T. Mukherjee, J.W. Elmer, J.O. Milewski, A. M. Beese, A. Wilson-Heid, A. De, W. Zhang, Additive manufacturing of metallic components – process, structure and properties, *Prog. Mater. Sci.* 92 (2018) 112–224.
- D. Huang, Y.P. Dong, H.C. Chen, Y.H. Zhou, M.X. Zhang, M. Yan, Effects of processing parameters on a β -solidifying TiAl alloy fabricated by laser-based additive manufacturing, *Microstructures* 2 (4) (2022) 2022019.
- K.G. Prashanth, S. Scudino, H.J. Klaus, K.B. Surreddi, L. Löber, Z. Wang, A. K. Chaubey, U. Kühn, J. Eckert, Microstructure and mechanical properties of Al–12Si produced by selective laser melting: effect of heat treatment, *Mater. Sci. Eng. A.* 590 (2014) 153–160.
- W.J. Chong, P. Wright, D.P. Simunec, S. Jayashree, W. Liew, C. Heazlewood, A. Trinchì, I. Kyratzis, Y. Li, S. Shen, A. Sola, C. Wen, A comprehensive study on the biodegradability, biocompatibility, and antibacterial properties of additively manufactured PLA-ZnO nanocomposites, *Smart Mater. Manuf.* 3 (2025) 100069.
- A. Takaichi, Suyalatu, T. Nakamoto, N. Joko, N. Nomura, Y. Tsutsumi, S. Migita, H. Doi, S. Kurosu, A. Chiba, N. Wakabayashi, Y. Igarashi, T. Hanawa, Microstructures and mechanical properties of Co–29Cr–6Mo alloy fabricated by selective laser melting process for dental applications, *J. Mech. Behav. Biomed. Mater.* 21 (2013) 67–76.
- K. Li, Z. Wang, K. Song, K. Khanlari, X.-S. Yang, Q. Shi, X. Liu, X. Mao, Additive manufacturing of a Co-Cr-W alloy by selective laser melting: in-situ oxidation, precipitation and the corresponding strengthening effects, *J. Mater. Sci. Technol.* 125 (2022) 171–181.
- X. Dong, Y. Zhou, Q. Sun, Y. Qu, H. Shi, W. Liu, H. Peng, B. Zhang, S. Xu, J. Yan, N. Li, Fatigue behavior of biomedical Co–Cr–Mo–W alloy fabricated by selective laser melting, *Mater. Sci. Eng. A.* 795 (2020) 140000.
- W.E. Frazier, Metal additive manufacturing: a review, *J. Mater. Eng. Perform.* 23 (6) (2014) 1917–1928.
- Y. Cao, W. Liu, L. Zhang, H. Sun, P. Bai, Preparation and properties of CoCrMo-Ni@Al₂O₃ composite by selective laser melting, *Mater. Charact.* 194 (2022) 112435.
- Z. Wang, S.Y. Tang, S. Scudino, Y.P. Ivanov, R.T. Qu, D. Wang, C. Yang, W. Zhang, A.L. Greer, J. Eckert, K.G. Prashanth, Additive manufacturing of a martensitic Co–Cr–Mo alloy: towards circumventing the strength–ductility trade-off, *Addit. Manuf.* 37 (2021) 101725.
- Q. Tan, H. Chang, G. Lindwall, E. Li, A. Durga, G. Liang, Y. Yin, G. Wang, M.-X. Zhang, Unravelling the roles of TiN-nanoparticle inoculant in additively manufactured 316 stainless steel, *J. Mater. Sci. Technol.* 175 (2024) 153–169.
- A.H. Karabacak, A. Çanakçı, S. Özkaya, S.A. Tunç, O. Güler, M. Çelebi, Effect of AlCrCuFeNi high entropy alloy reinforcements with and without B₄C on powder characteristic, mechanical and wear properties of AA5083 metal-metal composites, *J. Alloy. Compd.* 1008 (2024) 176627.
- Y.-l. Gu, M.-l. Yi, Y. Chen, J. Tu, Z.-m. Zhou, J.-r. Luo, Effect of the amount of SiC particles on the microstructure, mechanical and wear properties of FeMnCoCr high entropy alloy composites, *Mater. Charact.* 193 (2022) 112300.
- Y. Wang, Z. Liu, Y. Zhou, X. Yang, J. Tang, X. Liu, J. Li, G. Le, Microstructure and mechanical properties of TiN particles strengthened 316L steel prepared by laser melting deposition process, *Mater. Sci. Eng. A.* 814 (2021) 141220.
- V. Chak, H. Chattopadhyay, T.L. Dora, A review on fabrication methods, reinforcements and mechanical properties of aluminum matrix composites, *J. Manuf. Process.* 56 (2020) 1059–1074.
- Y. Zhao, M. Lu, Z. Fan, Y. Yin, W. Lin, H. Huang, Laser surface engineering of Ti–6Al–4V with TiO₂/Al₂O₃ composite powder for improved wear resistance, *Smart Mater. Manuf.* 1 (2023) 100015.
- B. Song, S. Dong, C. Coddet, Rapid in situ fabrication of Fe/SiC bulk nanocomposites by selective laser melting directly from a mixed powder of micronized Fe and SiC, *Scr. Mater.* 75 (2014) 90–93.
- Y. Li, H. Yan, B. Zhang, P. Zhang, H. Shi, Q. Lu, Investigating the influence of TiN on microstructural, mechanical, and tribological properties in selective laser melting of Inconel 718-based composites, *Mater. Today Commun.* 40 (2024) 110075.
- S. Thapliyal, P. Agrawal, P. Agrawal, S.S. Nene, R.S. Mishra, B.A. McWilliams, K. C. Cho, Segregation engineering of grain boundaries of a metastable Fe-Mn-Co-Cr-Si high entropy alloy with laser-powder bed fusion additive manufacturing, *Acta Mater.* 219 (2021) 117271.
- W. Zhai, W. Zhou, S.M.L. Nai, In-situ formation of TiC nanoparticles in selective laser melting of 316L with addition of micronized TiC particles, *Mater. Sci. Eng. A.* 829 (2022) 142179.
- C. Pan, D. Zhu, H. Luo, K. Kosiba, S. Qu, C. Yang, X. Li, Fabrication of high-performance CoCrNi medium entropy alloy by laser powder bed fusion: the effect of grain boundary segregation, *Compos. Part. B. Eng.* 253 (2023) 110540.
- W. Jiang, R. Li, J. He, S. Ni, L. Wang, Z. Chen, Y. Huang, C. Li, J. Yi, M. Song, Nitrogen-doping assisted local chemical heterogeneity and mechanical properties in CoCrMoW alloys manufactured via laser powder bed fusion, *Adv. Powder. Mater.* 3 (5) (2024) 100217.
- W. Jiang, X. An, S. Ni, L. Wang, J. He, Z. Chen, Y. Huang, M. Song, Achieving excellent strength-ductility combination through the control of intricate substructures in an additively manufactured Co–Cr–Mo alloy, *Mater. Sci. Eng. A.* 886 (2023) 145687.
- Y. Cao, W. Liu, Q. Xie, H. Sun, P. Bai, Strengthening mechanism of nickel coating in SLM processed Ni@Al₂O₃-CoCrMo composites, *Met. Mater. Intern.* 30 (6) (2024) 1687–1694.
- M. Isik, J.D. Avila, A. Bandyopadhyay, Alumina and tricalcium phosphate added CoCr alloy for load-bearing implants, *Addit. Manuf.* 36 (2020) 101553.
- A.M. Ribeiro, A.C. Alves, L.A. Rocha, F.S. Silva, F. Toptan, Synergism between corrosion and wear on CoCrMo–Al₂O₃ biocomposites in a physiological solution, *Tribol. Inter.* 91 (2015) 198–205.
- K. Yamanaka, M. Mori, A. Chiba, Effects of nitrogen addition on microstructure and mechanical behavior of biomedical Co–Cr–Mo alloys, *J. Mech. Behav. Biomed. Mater.* 29 (2014) 417–426.
- K. Yamanaka, M. Mori, A. Chiba, Nanoarchitected Co–Cr–Mo orthopedic implant alloys: nitrogen-enhanced nanostructure evolution and its effect on phase stability, *Acta Biomater.* 9 (4) (2013) 6259–6267.
- Z. Song, Y. Liu, Y. Liu, X. Jiang, D.G. Filipstou, A.V. Rogachev, Improving the protective properties of an artificial joint friction couple by using TiN and DLC films, *Surf. Coat. Technol.* 472 (2023) 129944.
- Y. Chen, X. Nie, A. Leyland, J. Housden, A. Matthews, Substrate and bonding layer effects on performance of DLC and TiN biomedical coatings in Hank's solution under cyclic impact-sliding loads, *Surf. Coat. Technol.* 237 (2013) 219–229.
- S. Piscane, L. Colombi Ciacchi, E. Vesselli, G. Comelli, O. Sbaizero, S. Meriani, A. De Vita, Bioactivity of TiN-coated titanium implants, *Acta Mater.* 52 (5) (2004) 1237–1245.

- [39] W. Cui, G. Qin, J. Duan, H. Wang, A graded nano-TiN coating on biomedical Ti alloy: low friction coefficient, good bonding and biocompatibility, *Mater. Sci. Eng. C*. 71 (2017) 520–528.
- [40] S. Ghosh, S. Abanteriba, Status of surface modification techniques for artificial hip implants, *Sci. Technol. Adv. Mater.* 17 (1) (2016) 715–735.
- [41] M. Sage, C. Guillaud, Méthode d'analyse quantitative des variétés allotropiques du cobalt par les rayons X, *Rev. Met. Paris* 47 (2) (1950) 139–145.
- [42] B. Wang, X. An, Z. Huang, M. Song, S. Ni, S. Liu, Nitrogen doped Co-Cr-Mo-W based alloys fabricated by selective laser melting with enhanced strength and good ductility, *J. Alloy. Compd.* 785 (2019) 305–311.
- [43] M. Cagirci, S. Guo, J. Ding, U. Ramamurty, P. Wang, Additive manufacturing of high-entropy alloys: current status and challenges, *Smart Mater. Manuf.* 2 (2024) 100058.
- [44] W. Abd-Elaziem, S. Elkatatny, A.-E. Abd-Elaziem, M. Khedr, M.A. Abd El-baky, M. A. Hassan, M. Abu-Okail, M. Mohammed, A. Järvenpää, T. Allam, A. Hamada, On the current research progress of metallic materials fabricated by laser powder bed fusion process: a review, *J. Mater. Res. Technol.* 20 (2022) 681–707.
- [45] X. Qi, X. Liang, J. Wang, H. Zhang, X. Wang, Z. Liu, Microstructure tailoring in laser powder bed fusion (L-PBF): strategies, challenges, and future outlooks, *J. Alloy. Compd.* 970 (2024) 172564.
- [46] M. Ghayoor, K. Lee, Y. He, C.-h. Chang, B.K. Paul, S. Pasebani, Selective laser melting of 304L stainless steel: role of volumetric energy density on the microstructure, texture and mechanical properties, *Addit. Manuf.* 32 (2020) 101011.
- [47] S. Zhao, X. Shen, J. Yang, W. Teng, Y. Wang, Densification behavior and mechanical properties of nanocrystalline TiC reinforced 316L stainless steel composite parts fabricated by selective laser melting, *Opt. Laser. Technol.* 103 (2018) 239–250.
- [48] D. Wei, A. Anniyaer, Y. Koizumi, K. Aoyagi, M. Nagasako, H. Kato, A. Chiba, On microstructural homogenization and mechanical properties optimization of biomedical Co-Cr-Mo alloy additively manufactured by using electron beam melting, *Addit. Manuf.* 28 (2019) 215–227.
- [49] R.A. Al-Aloosi, O. Çomaklı, M. Yazıcı, Z.A. Taha, Influence of scanning velocity on a CoCrMoW alloy built via selective laser melting: microstructure, mechanical, and tribological properties, *J. Mater. Eng. Perform.* 32 (15) (2023) 6717–6724.
- [50] J. Luo, W. Sun, R. Duan, W. Yang, K.C. Chan, F. Ren, X.-S. Yang, Laser surface treatment-introduced gradient nanostructured TiZrHfTaNb refractory high-entropy alloy with significantly enhanced wear resistance, *J. Mater. Sci. Technol.* 110 (2022) 43–56.
- [51] F.T. Mosisa, H.-W. Chen, Y.-L. Kuo, J.-Y. Guo, S.u. Mas'ud, W.-M. Hsu, Enhancing mechanical properties of surface hardness and abrasion resistance of Fe-Mn-Al alloy by using atmospheric pressure plasma jet nitriding, *Surf. Coat. Technol.* 484 (2024) 130817.
- [52] İ. Türkmen, E. Yalamaç, Effect of alternative boronizing mixtures on boride layer and tribological behaviour of boronized SAE 1020 steel, *Met. Mater. Int.* 28 (5) (2022) 1114–1128.
- [53] E. Mertgenç, Y. Kayalı, Ş. Talaş, Effect of boronizing and aluminizing on the wear resistance of steel AISI 1010, *Met. Sci. Heat. Treat.* 63 (7) (2021) 388–395.
- [54] Z. Dong, T. Zhou, J. Liu, X. Zhang, B. Shen, W. Hu, L. Liu, Effects of pack chromizing on the microstructure and anticorrosion properties of 316L stainless steel, *Surf. Coat. Technol.* 366 (2019) 86–96.
- [55] J. Zheng, G. Tang, F. Su, T. Li, Z. Liang, X. Liu, Facile fabrication of aluminium alloys with gradient nanostructures incorporating α -Al₂O₃ particles for enhanced tribological properties, *Tribol. Int.* 189 (2023) 108921.
- [56] S. Li, G. Tang, T. Zou, J. Wang, Z. Ou, H. Lin, F. Su, Z. Liang, Enhancing tribological properties of 18CrNiMo7-6 through grain refinement incorporating Al₂O₃ particles, *Tribol. Int.* 190 (2023) 109045.
- [57] N. Kantay, B. Rakhadilov, S. Kurbanbekov, D. Yeskermessov, G. Yerbolatova, A. Apezhanova, Influence of detonation-spraying parameters on the phase composition and tribological properties of Al₂O₃ coatings, *Coatings* 11 (2021) 793.
- [58] J.F. Archard, Contact and rubbing of flat surfaces, *J. Appl. Phys.* 24 (8) (1953) 981–988.